




Article

Light Hole Excitons in Strain-Coupled Bilayer Quantum Dots with Small Fine-Structure Splitting

Xiangjun Shang^{1,2,3} , Hanqing Liu^{1,2,3}, Xiangbin Su^{1,2,3}, Shulun Li^{1,2,3} , Huiming Hao^{1,2,3}, Deyan Dai^{1,2,3}, Zesheng Chen^{1,2,3}, Haiqiao Ni^{1,2,3} and Zhichuan Niu^{1,2,3,*} 

¹ State Key Laboratory for Superlattices and Microstructures, Institute of Semiconductors, Chinese Academy of Sciences, Beijing 100083, China

² Center of Materials Science and Optoelectronics Engineering, University of Chinese Academy of Sciences, Beijing 100049, China

³ Beijing Academy of Quantum Information Sciences, Beijing 100193, China

* Correspondence: zcnui@semi.ac.cn

Abstract: In this work, we measure polarization-resolved photoluminescence spectra from excitonic complexes in tens of single InAs/GaAs quantum dots (QDs) at the telecom O-band with strain-coupled bilayer structure. QDs often show fine-structure splitting (FSS) ~ 100 μeV in uniform anisotropy and valence-band mixing of heavy holes (HH) and light holes (LH); the biaxial strain also induces LH excitons with small FSS (especially XX, < 5 μeV , 70% of QDs); delocalized LH reduces the Coulomb interaction between holes V_{hh} and enhances population on LH excitons XX, XX_{11} , X_{11}^+ and XX_{21}^+ .

Keywords: strain-coupled bilayer QDs; fine-structure splitting; valence-band mixing; light hole



Citation: Shang, X.; Liu, H.; Su, X.; Li, S.; Hao, H.; Dai, D.; Chen, Z.; Ni, H.; Niu, Z. Light Hole Excitons in Strain-Coupled Bilayer Quantum Dots with Small Fine-Structure Splitting. *Crystals* **2022**, *12*, 1116. <https://doi.org/10.3390/cryst12081116>

Academic Editor: Shin-Tson Wu

Received: 9 July 2022

Accepted: 2 August 2022

Published: 10 August 2022

Publisher's Note: MDPI stays neutral with regard to jurisdictional claims in published maps and institutional affiliations.



Copyright: © 2022 by the authors. Licensee MDPI, Basel, Switzerland. This article is an open access article distributed under the terms and conditions of the Creative Commons Attribution (CC BY) license (<https://creativecommons.org/licenses/by/4.0/>).

1. Introduction

Epitaxial semiconductor quantum dots (QDs) can be uniformly fabricated in-plane with well-controlled growth parameters and optical performance, showing advantages in laser diodes and photodetectors [1–3]. In the quantum field, among various types of optically excited quantum emitters, single QDs in areal density $< 1 \times 10^9 \text{ cm}^{-2}$ cooled at temperature (T) < 60 K show multiple exciton states with discrete spectral lines; its micro-cavity integration for enhancement and coupling in single-mode fiber (with little chromatic or polarization mode dispersion) and photonic integrated circuit (PIC) [4–8] pave the way for information processing; telecom-band single photons enable 100-km fiber transmission and coupling in silicon-based PIC on mature silicon-on-insulator substrate. For QDs grown on GaAs substrate compatible with lattice-matched GaAs/Al(Ga)As distributed Bragg reflector (DBR) cavity to enhance vertical extraction, droplet and Stranski–Krastanov (S-K) epitaxy have proved single QDs in a wide wavelength (λ) range, 0.7–1.6 μm [9–12]. A delicate design of QD structures (e.g., QD size by deposition amount control [13], substrate orientation [14]/misorientation [15], strain-reducing layer (SRL) as cap or buffer [10,11,15,16], modulated doping [17–19] and tunneling [19]) is crucial for QD optical performance. Strain-coupled bilayer InAs QDs with the lower layer to create strain nucleation sites and the upper layer to form strain-relaxed larger QDs aligned, capped by InGaAs SRL, have proved single QDs at $\lambda \sim 1.3 \mu\text{m}$ [10]. Similar to its band tuning for high mobility [20], the strain engineering localized in the bilayer provides a tuning of exciton properties. Although photoluminescence (PL) study of QD ensembles has been fulfilled [21], a micro-PL (μPL) study of single QDs in such structure offers a direct probe to understand the strain effect on the QD electronic structure as referred to its morphology characterization and makes QD structure optimization more active. In this work, by extensive μPL study of many such kind of QDs in one sample in various exciton energies and configurations, it is found that the biaxial tensile strain in GaAs spacer below the upper QD induces a uniform QD anisotropy

with fine-structure splitting (FSS) ~ 100 μeV and light hole (LH) level with valence-band mixing (VBM) to heavy hole (HH) by tunneling (energy-dependent, higher-energy branch in a broader linewidth) as the degree of linear polarization (DLP) reflects [22]. LH excitons show that FSS is much reduced and becomes dominant when LHs delocalize, in particular biexciton XX_{LH} , with FSS as small as $0\sim 5$ μeV (70% of QDs), which is a little saturated under high pump when many LH excitons from the s-s or p-s transition in C_{3v} features are built by delocalized LHs, unlike a weak LH exciton in QD with a buried strain layer [23]. The delocalized LHs also reduce the FSS of HH excitons. Charge defects build an electric field to vary the FSS oscillation phase and reduce exciton formation, with a clear spectral shoulder originating from the phonon. While still posing challenges (e.g., careful control of strain and interface defect to enhance QD brightness, optimizing the microcavity to enhance extraction, adding a dielectric mask to avoid surface adsorption or scratch, etching mesa to reduce the bulk strain), the prospect of this hybrid quantum structure as a QD molecule [21,24] is encouraged.

2. Materials and Methods

The bilayer InAs QDs are grown in molecular beam epitaxy on semi-insulating GaAs (001) substrate with a gradient indium flux: ultralow deposition rate and higher T for the lower seed layer; higher deposition rate and lower T for the upper layer capped by a 5 nm $\text{In}_{0.15}\text{Ga}_{0.85}\text{As}$ SRL; a 8 nm GaAs layer between them acts as both cap and space with strain field to form aligned QDs; a planar GaAs/ $\text{Al}_{0.9}\text{Ga}_{0.1}\text{As}$ DBR cavity at $\lambda \sim 1.3$ μm ($Q \sim 400$) is integrated to enhance light extraction in this λ . For detail of the structure and growth, see [10,25]. To reflect QD size distribution, a test sample with the bottom DBR but no cavity filtering is grown to characterize the full spectrum of QDs and the atomic force microscope (AFM) morphology of uncapped QDs. Single-QD μPL spectrum is measured by a fiber-based confocal microscope spectrograph composed of an NA ~ 0.7 objective for collection with laser spot focused on the sample in diameter ~ 2 μm , a collimator coupling in single-mode fiber and a 0.5 m-long grating spectrometer equipped with a liquid nitrogen-cooled InGaAs linear array detector (Princeton Instruments). The sample is cooled at $T \sim 5$ K in a vibration-free helium-flow cryostat [26] and continuous-wave (cw) excited by a $\lambda = 632.8$ nm HeNe laser with the maximal power at the spot $P_0 \sim 50$ μW attenuated by a gradually varied neutral density filter for power-dependent measurement. A rotating half-wave plane (HWP) is inserted in front of a linear polarizer inline before fiber collection to filter out the distinct fine-structure component to observe energy oscillation beyond the spectrometer resolution, with peak energy of an exciton line in time-integrated PL spectra deduced from line fitting [17]. In the same QD, biexciton XX usually exhibits FSS oscillation in the same size but opposite sign to exciton X to emit polarization-correlated photon pairs. The LH–HH VBM [22] causes DLP, defined by $(I_x - I_y)/(I_x + I_y)$, where x and y mean two orthogonal axes, $[1\bar{1}0]$ and $[110]$. The slight offset in LH_x and LH_y is reflected from FSS oscillation too. To understand LH, QD band structure is simulated by *Nextnano* in 8-band $k\cdot p$ theory with elastic strain minimized. In fact, the bulk strain in a planar sample is significant to affect QD performance during cryogen cycles. Etching mesa will reduce bulk strain for a better control of QD condition for quantum emission.

3. Results

3.1. PL Spectra and AFM Images of Bilayer QDs

The bilayer QD growth is found to be more sensitive on indium surface migration driven by strain sites and growth T. In the test sample with capped and uncapped QDs, Figure 1 presents their AFM morphology and PL spectra. The statistics on QD AFM height show correspondence to their PL spectra: larger indium coverage in region 1 leads to individual QDs at $\lambda \sim 1.32$ μm at a height of ≥ 13 nm ($28/4$ μm^{-2}), while lower coverage in region 2 leads to fewer QDs at a height of ≥ 13 nm ($3/4$ μm^{-2}) and a strong profile at $\lambda \sim 1.05$ μm from dense QDs at a height of $9\sim 10$ nm. For single-layer QD growth with indium coverage increasing, the third critical coverage forms large QDs at $\lambda \sim 1.1$ μm and

1.2 μm with a quantized height of ~ 13 nm and 15 nm after the first one to form single QDs at $\lambda \sim 0.88$ μm at a height of 1–2 nm and the second one to form single QDs at $\lambda \sim 0.91$ μm at a height of 7–8 nm [13] after 2D–3D transition [27]. Here, the strain relaxation and possible interlayer level coupling form single QDs at a height of ~ 13 nm with redshift $\lambda \sim 1.3$ μm . The excited states [28] also appear as the arrows indicate. Their slight redshift in region 2 reflects sufficient migration to form larger QDs due to a higher T; in the wafer center (region 3) with much higher T and lower coverage, the λ of lower-density large QDs even extends to 1.36 μm . In AFM images, compared to region 1, region 2 with enhanced migration shows large QDs in a larger base and more small QDs at a height of 5–7 nm. For bright single-photon emission at $\lambda \sim 1.3$ μm , the lower T in region 1 to form defectless high-aspect-ratio QDs with exciton lines appearing in spectral profile is desired, i.e., purely strain-driven (instead of T-driven) surface migration. Single QDs can be filtered (spatially isolated) by DBR cavity (e.g., pillar) [26,29], in addition to good control of indium coverage and strain site (see the spectrum in black curve, i.e., another point in region 1, with individual QDs at $\lambda \sim 1.3$ μm in sharp exciton lines). Compared to the narrow growth T window for the bilayer single QDs at $\lambda \sim 1.3$ μm , the case is different for single QDs at $\lambda < 1.1$ μm , with the second critical coverage where a broad growth T exists (both region 1 and region 2 with various growth T show exciton lines in the spectral profile). QDs in the larger base likely have more interface defects to build a multielectric field to reduce exciton formation and show a smooth spectral profile from phonon broadening, with the excited states relatively higher populated. Since QD emission redshifts are ~ 100 nm at room T, the bilayer structure is also valuable for growth of QD ensemble at $\lambda \sim 1.45$ μm [12].

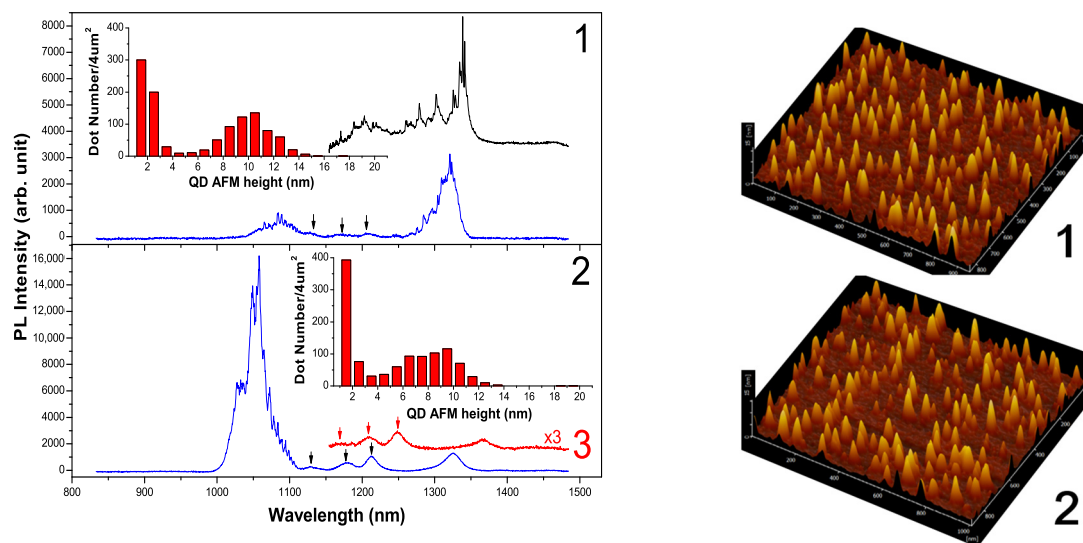


Figure 1. (left): μPL spectra of bilayer QDs: region 1 shows individual QDs at $\lambda \sim 1.32$ μm with exciton lines, two points, in blue and black curves; region 2 shows individual QDs at $\lambda \sim 1.32$ μm in lower aspect ratio and smooth spectral profile, a strong profile at $\lambda \sim 1.05$ μm from small QDs; region 3 shows extended λ ; (right): AFM images; (inset): statistics on QD AFM height.

3.2. Band Structure of Bilayer Single QD

The simulation result is presented in Figure 2. There are the electron, HH and LH ground states E1, LH1 and HH1; with proper QD size, their energy offsets agree with the emission $\lambda \sim 1.3$ μm . HH in p-type as simulated is localized in the upper QD, while LH in s-type is confined in the thin GaAs spacer below it where the biaxial tensile strain lifts the LH band. The biaxial strain mainly affects the valence band, enlarging HH anisotropy and FSS and building LH excitons in C_{3v} symmetry with small eh exchange (overlap) and FSS. An LH–HH mixing state as presented is responsible for DLP $\sim 30\%$ in polarization-resolved spectra below. The interlayer mixing is via LH tunneling (HH hardly tunnel), sensitive on its energy (i.e., spin states or polarization) and showing different spectral linewidths.

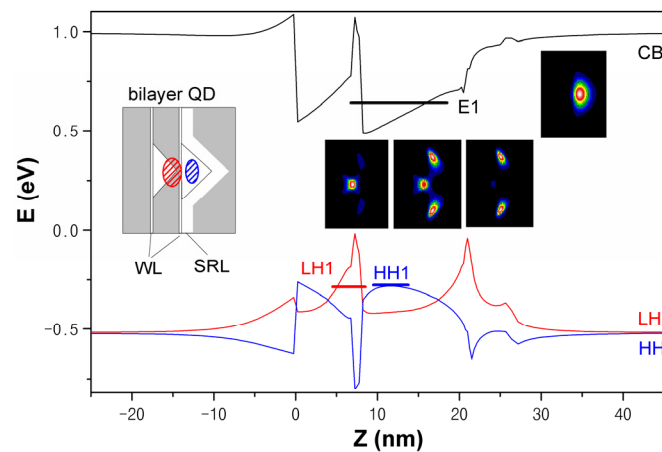


Figure 2. Band structure of bilayer QD as schematized (WL: wetting layer). Insets: ground-state wavefunctions.

3.3. QDs with Strain-Induced Large FSS

Figure 3 presents polarization-resolved PL spectra of six single-QDs in a planar DBR cavity in orthogonal axes, red [1–10] (horizontal, H) and black [110] (vertical, V). There are LHs and HHs to form HH excitons and LH excitons as marked, especially XX_{lh} . FSS $> 100 \mu\text{eV}$ in HH excitons X and XX with opposite signs reflect a large anisotropy in the bilayer QDs compared to single-layer QDs at $\lambda \sim 0.9 \mu\text{m}$ (FSS $\sim 30 \mu\text{eV}$ typically). The uniform FSS oscillation phases, lower-energy branch along 90° [110] V for X and 0° [1–10] H for XX, reflect a uniform QD elongation (or anisotropy) along [110] V formed by the biaxial strain. The dominant X shows different spectral linewidths in the two polarizations: higher-energy branch [1–10] H with more LH interlayer tunneling for mixing in a broader linewidth. XX with the two branches LH_X and LH_X filled shows the same linewidth in both polarizations. In the lower-energy side of X, there is an exciton in thinner linewidth with FSS ~ 0 , attributed to the negative trion X^- . For HH and LH biexcitons XX and XX_{lh} , there is an $XX_{1\bar{1}}$ ($2e1h_11h_2$) exciton in the lower-energy side with nearly equal energy offset. In QD2, QD4 and QD5, the $XX_{1\bar{1}}$ for HH (C_{2v} , LH h_2) shows negligible splitting, while the $XX_{1\bar{1}}$ for LH (C_{3v} , HH h_2) shows a splitting in the same oscillation phase as XX_{lh} , with FSS $\sim 37 \mu\text{eV}$ in QD5. In the higher-energy side, XX_{21}^+ ($2e2h_11h_2$) exciton shows a clear polarization feature, well-depicted by the C_{3v} transition scheme [30], which reflects the exchange Δ_{hh} between LH h_1 and HH h_2 : $\sim 150 \mu\text{eV}$ in QD1 and QD4 while $\sim 205 \mu\text{eV}$ in QD2, QD5 and QD6 with more LH interlayer coupling. More LH coupling broadens the exciton linewidth in QD2 and populates a dominant XX_{lh} in QD5 and QD6. In QD6, plenty of LH excitons in C_{3v} spectral features are located in both sides of XX_{lh} (FSS ~ 0) as mirror, e.g., XX_{21}^+ and $X_{1\bar{1}}^+$, $X_{0\bar{1}}$ and $XX_{1\bar{1}}$, $XX_{2\bar{1}}^+$ and $X_{1\bar{1}}^+$, reflecting higher symmetry; HH excitons X and XX are absent; the dominant XX_{lh} and X_{lh} show DLP $\sim 30\%$ related to VBM to HH h_2 . XX_{lh} usually shows FSS ~ 0 (QD1, QD3, QD4); in a charge field with LH interlayer coupling, it shows FSS $\sim 12 \mu\text{eV}$ nearly constant (also for X_{lh}) (see QD2, QD5 and QD6), which reflects the eh exchange energy Δ_{eh}^0 in the transition diagram [30]. In QD3 and QD4 with little coupling, the strain-induced LH–HH VBM shows the same DLP for X and XX, which is larger in QD3 with larger strain (DLP $\sim 30\%$, FSS $\sim 139 \mu\text{eV}$). In QD1 and QD2 with LH_X coupling and smaller FSS, XX shows larger DLP (30%) than X (DLP ~ 0). The negligible DLP in X is likely due to LH–HH VBM to the same LH_X with more coupling. XX_{lh} usually keeps the same DLP as XX (QD1, QD3, QD4). The LH delocalization usually reduces DLP. In QD2 (QD5) with more (less) LH coupling and smaller (larger) FSS, it shows smaller (larger) DLP than XX. The large DLP in XX_{lh} in QD5 is consistent with the DLP in X, reflecting polarization-related LH tunneling for mixing.

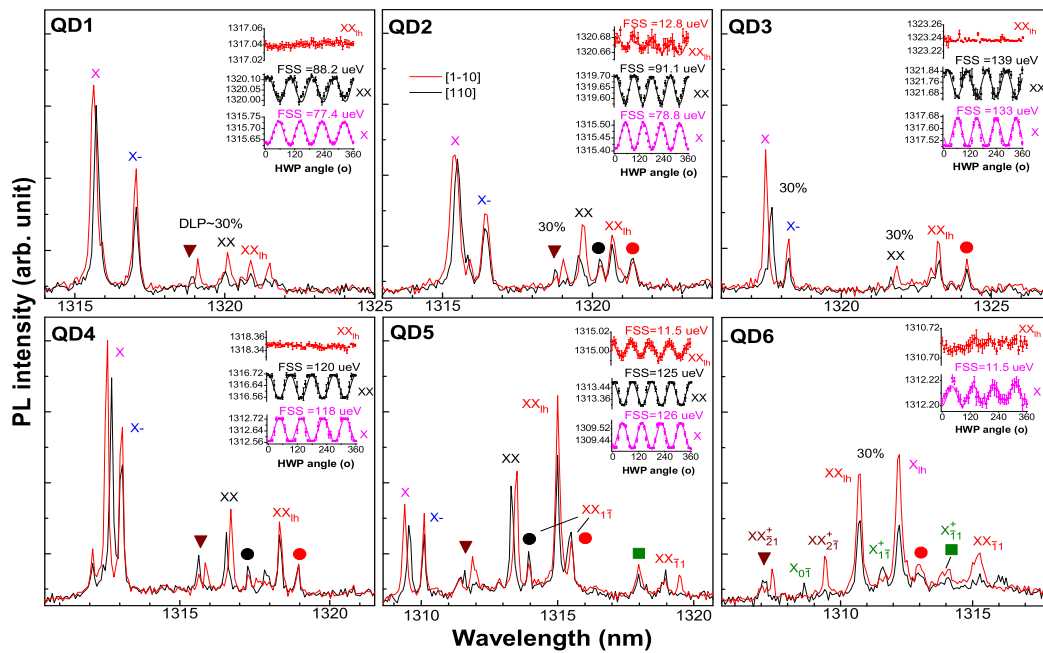


Figure 3. Polarization-resolved μ PL spectra of QD1–6 with large FSS, black and red: orthogonal axes [110] and [1–10], large DLP $\sim 30\%$ marked. (**Insets**): FSS oscillations. HH excitons X and XX in large FSS and opposite signs; LH excitons marked, especially XX_{lh} with small FSS, inverted triangle: XX_{21}^+ , circles: $XX_{1\bar{1}}$ for both HH and LH, square: $X_{1\bar{1}}^+$, QD6: more LH excitons located around XX_{lh} .

3.4. QDs with LH Excitons in Small FSS

Since LHs have small effective mass and shallow barriers (see Figure 2), a little variation of QD dielectric environment (e.g., interface charges) will reduce their barriers for interlayer delocalization and show dominant LH excitons such as XX and $X_{1\bar{1}}^+$ or XX_{21}^+ with HH excitons absent, see Figure 4. Unlike the QDs in Figure 3, here, related to the environment charge field, the FSS of the LH excitons XX and X varies from $<5 \mu\text{eV}$ to $22.6 \mu\text{eV}$, and higher excitons are populated. In pump-power dependence, the near-1 slopes for all excitons reflect a fluent hole capture in delocalized LHs. The identification of the exciton complex is based on their similar spectral features in different QDs as referred to transition diagram [30], their mirrored positioning as referred to QD6 and their pump-power dependence slopes. Apart from the dominant XX_{lh} , biexcitons XX_{21}^+ and $XX_{1\bar{1}}$ usually show larger slopes than excitons X, $X_{0\bar{1}}$, $X_{1\bar{1}}^+$, X^+ , X^- and $X_{0\bar{1}}^-$. Under low pump, in QD7 there are X, $X_{0\bar{1}}$, X^- , $X_{0\bar{1}}^-$ in slope ~ 0.82 or 0.88 , lower than $XX_{1\bar{1}}$ (~ 0.9); in QD8 there are $X_{1\bar{1}}^+$ and X in slopes ~ 0.93 or 0.74 , lower than XX (~ 1.05) and X^- (~ 0.84); in QD10 there are XX_{21}^+ and XX in slopes ~ 0.85 , higher than X (~ 0.83) and $X_{1\bar{1}}^+$ (~ 0.82). Under high pump, X and $X_{1\bar{1}}^+$ are lost in the background. Excitons X, $X_{0\bar{1}}$, $X_{1\bar{1}}^+$ and $X_{0\bar{1}}^-$ keep nearly the same FSS oscillation phase opposite to biexcitons. In QD7 with many delocalized LHs, XX_{lh} becomes like X^- with an additional delocalized LH attracted by Coulomb interaction, similar for the other excitons: XX_{21}^+ becomes $XX_{1\bar{1}}$, $XX_{1\bar{1}}$ becomes $X_{0\bar{1}}^-$, $X_{1\bar{1}}^+$ becomes $X_{0\bar{1}}$. Meanwhile, the X is kept and a positive trion X^+ appears at the $X_{1\bar{1}}^+$ position with a large positive binding energy $E_B = V_{eh} - V_{hh}$ (i.e., $V_{hh} \ll V_{eh}$) [31,32]. For spatially delocalized LH levels, their Coulomb interaction (V_{hh}) is greatly reduced and the hole–hole exchange Δ_{hh} tends to be negligible. In this case, XX_{21}^+ and $X_{1\bar{1}}^+$ in QD9 and QD10 show FSS ~ 0 ; $XX_{1\bar{1}}$ in QD7 (QD10) shows the same FSS as X (XX), reflecting Δ_{eh}^0 of $16\sim 17 \mu\text{eV}$. The Δ_{eh}^0 as FSS of X and XX reflect is $14\sim 22.6 \mu\text{eV}$ in the four QDs, a little larger than the Δ_{eh}^0 of the QDs in Figure 3, $\sim 12 \mu\text{eV}$; they will vary greatly in a strong defect field as QD13–15, reflected in Figure 5. There is also a tiny X peak near the new $XX_{1\bar{1}}$, similar as QD8 and QD10. In QD10, different spectral features of $XX_{1\bar{1}}$ and $XX_{1\bar{1}}$ are clearly shown, as referred to C_{3v} transition schemes [30]. In QD7 with $\Delta_{hh} \sim 0$, the FSS $\sim 40.5 \mu\text{eV}$ in $X_{0\bar{1}}$ reflects Δ_{eh}^1 ($e-h_2$) [30]. In QD8 with less LH delocalization, apart from the dominant XX_{lh} (FSS $\sim 4.9 \mu\text{eV}$ with an additional

LH_Z with FSS ~ 0), there is a dominant $X_{1\bar{1}}^+$ with FSS ~ 45.3 μeV and a secondary $XX_{1\bar{1}}$ with FSS ~ 56.3 μeV in opposite oscillations, reflecting a large $\Delta_{\text{hh}} \sim 70$ μeV with slight energy difference in $\Delta_{\text{eh}}^0 \sim 14.1$ μeV ($e-h_1$) and $\Delta_{\text{eh}}^I \sim 25$ μeV ($e-h_2$) in C_{3v} transition diagram [30]. QD7, QD9 and QD10 with delocalized LHs show population on XX_{21}^+ and other higher excitons located around XX_{1h} (see QD9). In QD10, the hydrostatic charge field is high enough to vary the FSS oscillation phase and show a dominant $XX_{1\bar{1}}$ (i.e., X^- coupled with an additional delocalized LH by Coulomb attraction) under high pump. In QD6~10 with LH delocalization, XX shows a negative E_B (also X^- in QD7, QD8, QD10, $E_B = V_{eh} - V_{ee}$) from smaller V_{eh} , $V_{eh} \lesssim V_{ee}$. In one sample, both QDs (large FSS and VBM or small FSS and LH exciton) will be found. To illustrate the small FSS in XX_{1h} , Figure 5 presents QD11~15. Unlike QD11 and QD12, QD13~15 with a hydrostatic charge field as screening show a weak exciton intensity with the FSS oscillation shift (lower-energy XX branch in [110]) and a clear spectral shoulder from the phonon. Around the minimum FSS ~ 0 , the charge field varies the FSS oscillation phase quickly [33], e.g., 2.1 μeV in QD13. In QD15, the dominant XX with larger FSS shows oscillation shift clearly. For a more delocalized LH wavefunction, the tuning of FSS needs a higher charge field, and thus there are $\sim 70\%$ of QDs show XX_{1h} FSS < 5 μeV as the statistics in Figure 5 reflect.

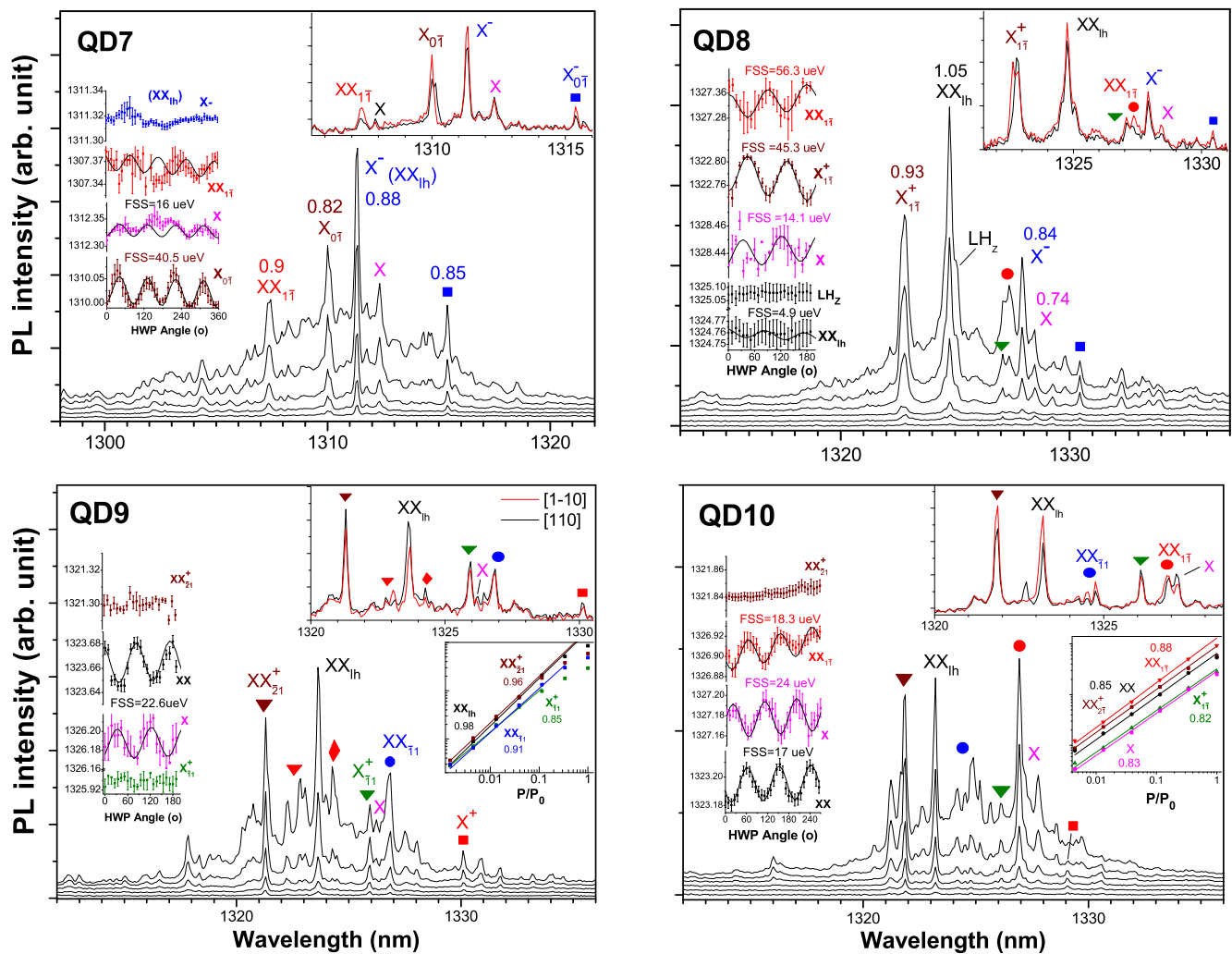


Figure 4. Pump-power-dependent μPL spectra of QD7–10 with LH excitons in small FSS. Inverted triangles: XX_{21}^+ (wine), $X_{1\bar{1}}^+$ (green), circles: $XX_{1\bar{1}}$ (red), $XX_{1\bar{1}}$ (blue), squares: X^+ (red), $X_{0\bar{1}}^-$ (blue), pink: X , black: XX_{1h} , red diamond in QD9: higher excitons. (Insets: left): FSS oscillations; (top-right): polarization-resolved spectra; (bottom-right): pump-power dependence, slope marked in plot or near peak.

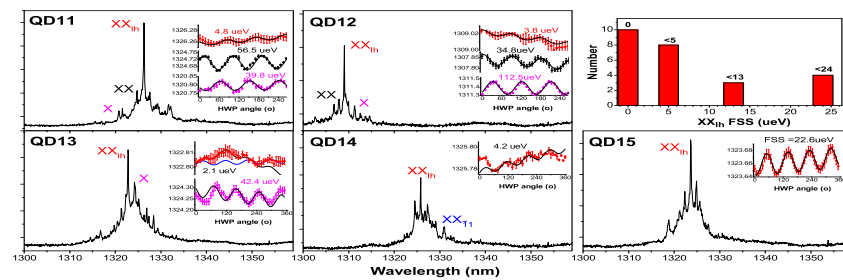


Figure 5. μ PL spectra of QD11–15 with dominant XX_{lh} in various FSS. QD13–15 with charge field to vary FSS oscillation phase and show phonon-related spectral shoulder. QD14 in similar spectrum as QD9. (**Top-right**): statistics on XX_{lh} FSS as measured.

4. Conclusions

In this work, by microphotoluminescence (μ PL) spectroscopy of bilayer single QDs, the strain effect on QD electronic structure, anisotropy, light hole (LH) formation and interlayer coupling have been uncovered from the spectral features, fine-structure splitting (FSS) and the degree of linear polarization. The biaxial strain enlarges QD anisotropy in $[110]$ for large FSS ~ 100 μ eV. It also induces LH excitons with small FSS (especially XX with FSS < 5 μ eV, 70% of QDs). LH interlayer coupling greatly reduces the FSS of HH excitons with mixing and leads to dominant population on LH excitons XX , XX_{11} and XX_{21}^+ . If there are charge defects at the QD interface to build hydrostatic multi-electric fields, the exciton formation will be reduced and the emission from single QD will show an obvious spectral profile from the phonon scattering broadening; besides, the electric fields also vary the FSS oscillation phase. The μ PL study combined with AFM morphology facilitates the optimization and the growth of the hybrid QD structure.

Author Contributions: X.S. (Xiangjun Shang), H.L., X.S. (Xiangbin Su), S.L., H.H. and D.D. took part in the optical measurement; H.L., X.S. (Xiangbin Su), Z.C. and H.N. took part in the sample growth; X.S. (Xiangjun Shang) and H.L. wrote the manuscript; Z.C., H.H., D.D. and H.N. participated in the discussions; H.N. and Z.N. supervised the writing of manuscript. All authors have read and agreed to the published version of the manuscript.

Funding: This research work is supported by the National Key Technologies R&D Program of China (Grant No. 2018YFA0306100), the Science and Technology Program of Guangzhou (Grant No. 202103030001), the Key-Area Research and Development Program of Guangdong Province (Grant No. 2018B030329001), the National Natural Science Foundation of China (Grant Nos. 62035017, 61505196), the Scientific Instrument Developing Project of Chinese Academy of Sciences (Grant No. YJKYYQ20170032), and the Program of Beijing Academy of Quantum Information Sciences (Grant No. Y18G01).

Institutional Review Board Statement: Not applicable.

Informed Consent Statement: Not applicable.

Data Availability Statement: The data that support the findings of this study are available from the corresponding author upon reasonable request.

Conflicts of Interest: The authors declare no conflict of interest.

References

1. Huffaker, D.L.; Park, G.; Zou, Z.; Shchekin, O.B.; Deppe, D.G. 1.3 μ m room-temperature GaAs-based quantum-dot laser. *Appl. Phys. Lett.* **1998**, *73*, 2564. [\[CrossRef\]](#)
2. Chen, S.; Li, W.; Wu, J.; Jiang, Q.; Tang, M.; Shutts, S.; Elliott, S.; Sobiesierski, A.; Seeds, A.; Ross, I.; et al. Electrically pumped continuous-wave III–V quantum dot lasers on silicon. *Nat. Photon.* **2016**, *10*, 307–311. [\[CrossRef\]](#)
3. Liu, H.C.; Gao, M.; McCaffrey, J.; Wasilewski, Z.R.; Fafard, S. Quantum dot infrared photodetectors. *Appl. Phys. Lett.* **2001**, *78*, 79. [\[CrossRef\]](#)

4. Shang, X.-J.; Li, S.-L.; Liu, H.-Q.; Su, X.-B.; Hao, H.-M.; Dai, D.-Y.; Li, X.-M.; Li, Y.-Y.; Gao, Y.-F.; Dou, X.-M.; et al. Single- and Twin-Photons Emitted from Fiber-Coupled Quantum Dots in a Distributed Bragg Reflector Cavity. *Nanomaterials* **2022**, *12*, 1219. [\[CrossRef\]](#)
5. Chen, Y.; Li, S.-L.; Shang, X.-J.; Su, X.-B.; Hao, H.-M.; Shen, J.-X.; Zhang, Y.; Ni, H.-Q.; Ding, Y.; Niu, Z.-C. Fiber coupled high count-rate single-photon generated from InAs quantum dots. *J. Semicond.* **2021**, *42*, 072901. [\[CrossRef\]](#)
6. Bauer, S.; Wang, D.; Hoppe, N.; Nawrath, C.; Fischer, J.; Witz, N.; Kaschel, M.; Schweikert, C.; Jetter, M.; Portalupi, S.L.; et al. Achieving stable fiber coupling of quantum dot telecom C-band single-photons to an SOI photonic device. *Appl. Phys. Lett.* **2012**, *119*, 211101. [\[CrossRef\]](#)
7. Pooley, M.A.; Ellis, D.J.P.; Patel, R.B.; Bennett, A.J.; Chan, K.H.A.; Farrer, I.; Ritchie, D.A.; Shields, A.J. Controlled-NOT gate operating with single photons. *Appl. Phys. Lett.* **2012**, *100*, 211103. [\[CrossRef\]](#)
8. Papon, C.; Zhou, X.-Y.; Thyrestrup, H.; Liu, Z.; Stobbe, S.; Schott, R.; Wieck, A.D.; Ludwig, A.; Lodahl, P.; Midolo, L. Nanomechanical single-photon routing. *Optica* **2019**, *6*, 524. [\[CrossRef\]](#)
9. Huo, Y.H.; Rastelli, A.; Schmidt, O.G. Ultra-small excitonic fine structure splitting in highly symmetric quantum dots on GaAs (001) substrate. *Appl. Phys. Lett.* **2013**, *102*, 152105. [\[CrossRef\]](#)
10. Chen, Z.-S.; Ma, B.; Shang, X.-J.; He, Y.; Zhang, Y.L.-C.; Ni, H.-Q.; Wang, J.-L.; Niu, Z.-C. Telecommunication Wavelength-Band Single-Photon Emission from Single Large InAs Quantum Dots Nucleated on Low-Density Seed Quantum Dots. *Nanoscale Res. Lett.* **2016**, *11*, 382. [\[CrossRef\]](#)
11. Sapienza, L.; Malein, R.N.; Kuklewicz, C.E.; Kremer, P.E.; Srinivasan, K.; Griffiths, A.; Clarke, E.; Gong, M.; Warburton, R.J.; Gerardot, B.D. Exciton fine-structure splitting of telecom-wavelength single quantum dots: Statistics and external strain tuning. *Phys. Rev. B* **2013**, *88*, 155330. [\[CrossRef\]](#)
12. Sittig, R.; Nawrath, C.; Kolatschek, S.; Bauer, S.; Schaber, R.; Huang, J.; Vijayan, P.; Pruy, P.; Portalupi, S.L.; Jetter, M.; et al. Thin-film InGaAs metamorphic buffer for telecom C-band InAs quantum dots and optical resonators on GaAs platform. *Nanophotonics* **2022**, *11*, 1109. [\[CrossRef\]](#)
13. Shang, X.-J.; Xu, J.-X.; Ma, B.; Chen, Z.-S.; Wei, S.-H.; Li, M.-F.; Zha, G.-W.; Zhang, L.-C.; Yu, Y.; Ni, H.-Q.; et al. Proper In deposition amount for on-demand epitaxy of InAs/GaAs single quantum dots. *Chin. Phys. B* **2016**, *25*, 107805. [\[CrossRef\]](#)
14. Kuroda, T.; Mano, T.; Ha, N.; Nakajima, H.; Kumano, H.; Urbaszek, B.; Jo, M.; Abbarchi, M.; Sakuma, Y.; Sakoda, K.; et al. Symmetric quantum dots as efficient sources of highly entangled photons: Violation of Bell's inequality without spectral and temporal filtering. *Phys. Rev. B* **2013**, *101*, 041306. [\[CrossRef\]](#)
15. Liang, S.; Zhu, H.L.; Ye, X.L.; Wang, W. Effect of GaAs (100) 2° surface misorientation on the formation and optical properties of MOCVD grown InAs quantum dot. *Appl. Surf. Sci.* **2006**, *252*, 8126. [\[CrossRef\]](#)
16. Shriram, S.R.; Kumar, R.; Panda, D.; Saha, J.; Tongbram, B.; Mantri, M.R.; Gazi, S.A.; Mandal, A.; Chakrabarti, S. Study on Inter Band and Inter Sub-Band Optical Transitions With Varying InAs/InGaAs Sub-Monolayer Quantum Dot Heterostructure Stacks Grown by Molecular Beam Epitaxy. *IEEE Trans. Nanotechnol.* **2020**, *19*, 601. [\[CrossRef\]](#)
17. Shang, X.-J.; Li, S.-L.; Liu, H.-Q.; Ma, B.; Su, X.-B.; Chen, Y.; Shen, J.-X.; Hao, H.-M.; Liu, B.; Dou, X.-M.; et al. Symmetric Excitons in an (001)-Based InAs/GaAs Quantum Dot Near Si Dopant for Photon-Pair Entanglement. *Crystal* **2021**, *11*, 1194. [\[CrossRef\]](#)
18. Shang, X.-J.; Ma, B.; Ni, H.-Q.; Chen, Z.-S.; Li, S.-L.; Chen, Y.; He, X.-W.; Su, X.-L.; Shi, Y.-J.; Niu, Z.-C. C_{2v} and D_{3h} symmetric InAs quantum dots on GaAs (001) substrate: Exciton emission and a defect field influence. *AIP Adv.* **2020**, *10*, 085126. [\[CrossRef\]](#)
19. Fathpour, S.; Mi, Z.; Bhattacharya, P. High-speed quantum dot lasers. *J. Phys. D Appl. Phys.* **2005**, *38*, 2103. [\[CrossRef\]](#)
20. Thompson, S.E.; Armstrong, M.; Auth, C.; Cea, S.; Chau, R.; Glass, G.; Hoffman, T.; Klaus, J.; Ma, Z.; McIntyre, B.; et al. A Logic Nanotechnology Featuring Strained-Silicon. *IEEE Electron Device Lett.* **2004**, *25*, 191. [\[CrossRef\]](#)
21. William, E.K.; Pancholi, A.; Stoleru, V.G. Quantum dot molecules: A potential pathway towards terahertz devices. *Phys. E Low-Dimens. Syst. Nanostruct.* **2006**, *35*, 139.
22. Belhadj, T.; Amand, T.; Kunold, A.; Simon, C.-M.; Kuroda, T.; Abbarchi, M.; Mano, T.; Sakoda, K.; Kunz, S.; Marie, X.; et al. Impact of heavy hole-light hole coupling on optical selection rules in GaAs quantum dots. *Appl. Phys. Lett.* **2010**, *97*, 051111. [\[CrossRef\]](#)
23. Zhang, J.-X.; Huo, Y.-H.; Rastelli, A.; Zopf, M.; Höfer, B.; Chen, Y.; Ding, F.; Schmidt, O.G. Single photons On-demand from light-hole excitons in strain-engineered quantum dots. *Nano. Lett.* **2015**, *15*, 422. [\[CrossRef\]](#)
24. Beirne, G.J.; Hermannstadter, C.; Wang, L.; Rastelli, A.; Schmidt, O.G.; Michler, P. Quantum Light Emission of Two Lateral Tunnel-Coupled (In, Ga)As/GaAs Quantum Dots Controlled by a Tunable Static Electric Field. *Phys. Res. Lett.* **2006**, *96*, 137401. [\[CrossRef\]](#) [\[PubMed\]](#)
25. Chen, Z.-S.; Ma, B.; Shang, X.-J.; Ni, H.-Q.; Wang, J.-L.; Niu, Z.-C. Bright single-photon source at 1.3 um based on InAs bilayer quantum dot in micropillar. *Nanoscale Res. Lett.* **2017**, *12*, 378. [\[CrossRef\]](#)
26. Li, S.-L.; Shang, X.-J.; Chen, Y.; Su, X.-B.; Hao, H.-M.; Liu, H.-Q.; Zhang, Y.; Ni, H.-Q.; Niu, Z.-C. Wet-etched microlens array for 200 nm spatial isolation of epitaxial single QDs and 80 nm broadband enhancement of their quantum light extraction. *Nanomaterials* **2021**, *11*, 1136. [\[CrossRef\]](#) [\[PubMed\]](#)
27. Li, M.-F.; Yu, Y.; He, J.-F.; Wang, L.-J.; Zhu, Y.; Shang, X.-J.; Ni, H.-Q.; Niu, Z.-C. In situ accurate control of 2D-3D transition parameters for growth of low-density InAs/GaAs self-assembled quantum dots. *Nanoscale Res. Lett.* **2013**, *8*, 86. [\[CrossRef\]](#) [\[PubMed\]](#)
28. Alloing, B.; Zinoni, C.; Li, L.H.; Fiore, A.; Patriarche, G. Structural and optical properties of low-density and In-rich InAs/GaAs quantum dots. *J. Appl. Phys.* **2007**, *101*, 024918. [\[CrossRef\]](#)

-
29. Yamaguchi, T.; Tawara, T.; Kamada, H.; Gotoh, H.; Okamoto, H.; Nakano, H.; Mikami, O. Single-photon emission from single quantum dots in a hybrid pillar microcavity. *Appl. Phys. Lett.* **2008**, *92*, 081906. [[CrossRef](#)]
 30. Karlsson, K.F.; Oberli, D.A.; Dupertuis, M.; Troncale, V.; Byszewski, M.; Pelucchi, E.; Rudra, A.; Holtz, P.O.; Kapon, E. Spectral signatures of high-symmetry quantum dots and effects of symmetry breaking. *New J. Phys.* **2015**, *17*, 103017. [[CrossRef](#)]
 31. Kettler, J.; Paul, M.; Olbrich, F.; Zeuner, K.; Jetter, M.; Michler, P. Neutral and charged biexciton-exciton cascade in near-telecom-wavelength quantum dots. *Phys. Rev. B* **2016**, *94*, 045303. [[CrossRef](#)]
 32. Carmesin, C.; Olbrich, F.; Mehrtens, T.; Florian, M.; Michael, S.; Schreier, S.; Nawrath, C.; Paul, M.; Höschele, J.; Gerken, B.; et al. Structural and optical properties of InAs/(In)GaAs/GaAs quantum dots with single-photon emission in the telecom C-band up to 77 K. *Phys. Rev. B* **2016**, *98*, 125407. [[CrossRef](#)]
 33. Trotta, R.; Zallo, E.; Ortix, C.; Atkinson, P.; Plumhof, J.D.; van den Brink, J.; Rastelli, A.; Schmidt, O.G. Universal Recovery of the Energy-Level Degeneracy of Bright Excitons in InGaAs Quantum Dots without a Structure Symmetry. *Phys. Rev. Lett.* **2012**, *109*, 147401. [[CrossRef](#)]